Ultrasonics Sonochemistry 97 (2023) 106444

Contents lists available at ScienceDirect

Ultrasonics Sonochemistry

journal homepage: www.elsevier.com/locate/ultson

Understanding the ultrasound field of high viscosity mixtures: Experimental and numerical investigation of a lab scale batch reactor

Ariana Bampouli [a], Quinten Goris [a], Jonas Van Olmen [a], Serkan Solmaz [a], Mohammed Noorul Hussain [a], Georgios D. Stefanidis [b], Tom Van Gerven [a,*]

[a] Department of Chemical Engineering, Process Engineering for Sustainable Systems, KU Leuven, Celestijnenlaan 200F, 3001 Heverlee, Belgium
[b] School of Chemical Engineering, Department of Process Analysis and Plant Design, National Technical University of Athens, Iroon Polytecneiou 9, Zografou 15780, Athens, Greece

ARTICLE INFO

Keywords:
Acoustic cavitation
Wave attenuation
Numerical simulation
Viscosity effect
Calorimetry
Sonochemiluminescence
Particle image velocimetry

ABSTRACT

In this work, mixtures of increasing viscosity (from 0.9 to ≈720 mPas) are sonicated directly using an ultrasonic horn at 30 kHz to investigate the effect of viscosity on the ultrasound field both from an experimental and numerical point of view. The viscosity of the mixtures is modified by preparing water-polyethylene glycol solutions. The impact of the higher viscosity on the acoustic pressure distribution is studied qualitatively and semi-quantitatively using sonochemiluminescence. The velocity of light scattering particles added in the mixtures is also explored to quantify acoustic streaming effects using Particle Image Velocimetry (PIV). A numerical model is developed that is able to predict cavitationally active zones accounting for both thermoviscous and cavitation based attenuation. The results show that two cavitation zones exist: one directly under the horn tip and one around the part of the horn body that is immersed in the liquid. The erosion patterns on aluminum foil confirm the existence of both zones. The intensity of the cavitationally active zones decreases considerably with increasing viscosity of the solutions. A similar reduction trend is observed for the velocity of the particles contained in the jet directly under the tip of the horn. Less erratic flow patterns relate to the high viscosity mixtures tested. Finally, two numerical models were made combining different boundary conditions related to the ultrasonic horn. Only the model that includes the radial horn movements is able to qualitatively predict well the location of the cavitation zones and the decrease of the zones intensity, for the highest viscosities studied. The current findings should be taken into consideration in the design and modelling phase of horn based sonochemical reactors.

1. Introduction

The implementation of ultrasound (US) as an energy source during preparation, processing or post-processing steps has been reported for various applications including chemicals and polymers synthesis, waste water treatment, crystallization, separation processes and biotechnological applications among others [1,2]. Studies focusing on the processing of high viscosity products, such as polymers, have reported many advantages when sonication is applied. Specifically, US can assist the initiation of polymerization reactions, by enabling better dispersion of the reactants, improving the mixing and heating of the bulk, resulting in increase of the reaction rate [3]. Conventionally, thermal or photochemical decomposition of pure monomers or added initiators is applied for the initiation of polymerization reactions [4]. As an alternative, application of US has been associated with the production of radical species that are able to initiate polymerization reactions [5].

The main effects of US are coupled with a phenomenon known as *cavitation*, i.e. the formation, growth and violent collapse of micro bubbles in the liquid medium which are accompanied by localized temperature and pressure hotspots [1,6,7]. Appropriate conditions are necessary for cavitation to occur, specifically the acoustic pressure generated by the ultrasound field needs to exceed the cavitation threshold pressure [7,8]. Cavitation further triggers a series of other phenomena, such as acoustic streaming, high shear stress, mixing in micro-scale, free radicals formation, boundary layer disruption and turbulence at a very local, small scale [1,3,9]. Despite the potential of US processing, the accurate prediction of the non-uniform distribution of cavitational activity in a reactor is challenging and therefore becomes a

* Corresponding author.
E-mail address: tom.vangerven@kuleuven.be (T. Van Gerven).

https://doi.org/10.1016/j.ultsonch.2023.106444
Received 17 January 2023; Received in revised form 21 April 2023; Accepted 15 May 2023
Available online 23 May 2023

major restriction for scaling up even the most promising processes [1,9–11].

Various qualitative and quantitative methods are available in order to characterize the sonochemical activity inside a reactor. Possible effects related to the sonication of a medium include acoustic pressure and local temperature increase [12], viscosity decrease and free radicals formation due to water dissociation [13]. Physical and physicochemical effects, such as the modification of solid surfaces, are also possible [13,14]. The process of investigating cavitation related activity is referred to as *mapping*. According to Sutkar and Gogate [1], this process can experimentally estimate both primary (e.g. temperature and pressure measurement) and secondary (e.g. iodine dosimetry, sonochemiluminescence of luminol, aluminum foil erosion, polymer degradation, among others) effects. Nevertheless, many of these techniques are interfering with the liquid medium during the measurement. An example is in the case of pressure measurements with a hydrophone, whereas the precise measurement of the cavitation active zones is for most cases not feasible [1,9,10,15].

Alternatively, theoretical models can be applied for the prediction of elevated pressure zones and for the calculation of the energy dissipation of sound waves in a bubbly medium. Models based on non-linear differential equations have been proposed by Van Wijngaarden [16], Caflish et al., [17] and Louisnard [18]. At the same time, a number of studies have been published based on linearization [7,10,12,19,20]. Simplified linear equations aim at facilitating implementation and reducing the overall computational requirements. Nevertheless, rigorous prediction of the acoustic pressure field remains challenging due to its coupling with the cavitational activity and its dynamic behavior [1,9,10,18,21]. Specifically, the acoustic energy of a travelling US wave inside a medium is lowered due to attenuation. The damping is caused by the cavitation activity or the presence of cavitation bubbles, which are generated by high acoustic pressure [10,22,23], and will be termed as "cavitation based attenuation" herein. The presence of gas cavitation bubbles results not only in sound attenuation, but also in considerable change of the velocity of the interacting phases [8]. Another important factor causing acoustic energy depreciation is the viscosity of the medium [24], which will be referred to as "thermoviscous attenuation" herein [25,26]. Incorporation of attenuation in a numerical model is undoubtedly improving the accuracy of the acoustic field distribution prediction. Nevertheless, in some studies, the complexity of including attenuation has been avoided by completely neglecting it [7]. When cavitation based attenuation due to the nonlinear bubble oscillations is taken into account, the linear Commander and Prosperetti model [19], combined with an also linear Helmholtz wave equation has often been implemented [10,22]. A drawback of applying linearization is the underestimation of damping, especially in transient cavitation regimes. The existing literature has shown however, that numerical simulations based on the Commander and Prosperetti model are able to predict the foreseen locations of transient cavitation [22], enable the estimation of the pressure field distribution [15,27] and assist in the optimal sonication conditions selection [28].

The liquid properties, with viscosity in particular, and the presence of bubbles are important factors for the estimation of attenuation during wave propagation [10,29]. In the study of Louisnard [18] for example, it was mentioned that viscous dissipation is one of the dominant factors significantly affecting cavitation based attenuation and wave propagation. Surprisingly, there are not many examples of studies that have investigated the impact of the medium's viscosity modification in combination with the presence of cavitation bubbles. Furthermore, the numerical and experimental investigation of such a system has not yet been reported. Therefore the current study aims in filling this gap by a novel approach, summarized as follows:

- Building up from water to higher viscosity mixtures (experimentally prepared by the authors)
- Identification of cavitationally active zones location and estimation of the acoustic pressure by numerical simulations coupled with experimental validation
- Combination of cavitation based and thermoviscous attenuation, using correct boundary conditions for the US source in the numerical model
- Experimental investigation of the impact of viscosity on acoustic streaming in cavitating liquid

An ultrasonic horn type device operating at 30 kHz was used to sonicate the prepared solutions. The choice for low operating frequency enabled maintaining high cavitation activity in the system, The cavitational activity of various, increasing viscosity mixtures was compared quantitatively by calorimetry measurements. Particle image velocimetry was also used to evaluate the impact of the medium's viscosity on the particle displacement. The sonochemiluminescence method was employed to visualise firstly, the location of active cavitation zones and secondly, the influence of viscosity on the zones intensity. A numerical model was prepared in COMSOL Multiphysics, and proved able to predict the location and intensity of the cavitation zones when compared against obtained experimental results. The addition of such a numerical tool aims in reducing the dependency on lab experiments and ease up the design and operation of sonochemically aided reactors used for the processing of high viscosity mixtures.

The manuscript starts with the experimental methods for obtaining the necessary properties of the investigated mixtures in Section 2, followed by the theoretical background in Section 3 including the equations used for modelling of the wave propagation and the model set up details. The results are discussed in Section 4. Lastly, conclusions and future perspectives are included in Section 5.

2. Experimental section

2.1. Materials

Water and polyethylene glycol (PEG) of varying molecular weight, were thoroughly mixed in different mass fractions for the preparation of solutions with increasing viscosity. PEG with number average molecular weight of 400 g/mol (maximum water content 0.5%) was purchased from Sigma Aldrich. PEG with molecular weight 2000, 4000, 8000 and 20000 g/mol (purity $>$ 99.5%) were provided by Clariant. The glycols will be named "PEG400", "PEG2000", "PEG4000", "PEG8000" "PEG20000" for simplicity hereafter. For the sonochemiluminescence method, luminol with purity $>$ 96.5% was purchased from Sigma Aldrich and sodium hydroxide (micro pearls for analysis) from Acros Organics. Fluorescent particles for Micro-PIV applications (PMMA coated with Rhodamine B, diameter 20 – 50 μm powder) from LaVision were used for the particles image velocimetry experiments. All chemicals were used as received. MilliQ water (18.2 MΩcm) was used for the preparation of the solutions.

2.2. Properties measurement

The ***viscosity*** (μ) ***and density*** (ρ) measurements were obtained simultaneously using an Anton Paar Lovis 2000 ME/DMA 4500 viscodensity meter. The density measuring principle relied on an oscillating U-tube sensor. Samples were carefully loaded on the tube, in order to eliminate bubble formation that would distort the measurement. The viscosity measurement relied on the determination of the rolling time of a golden ball through a capillary of known diameter filled with the sample of interest. The inclination angle of the capillary was chosen, while the optimal capillary diameter was determined via trial and error. Similar to the density measurements, sample loading was done carefully to avoid bubbles inside the capillary. A temperature scan was performed via a Peltier temperature control, from 23 °C to 88 °C in steps of 5 °C per measurement. It should be noted that the temperature steps were

decreased to 2.5 °C for the lowest concentration samples (10 wt%).

The ***isobaric specific heat values*** (c_p) were obtained using a DSC-Q2000 from TA Instruments. The DSC cell was purged with nitrogen gas at a flowrate of 50 ml/min. Samples of approximately 8-10 mg were placed in sealed aluminum pans. Samples were measured while being heated and subsequently cooled at 10 °C /min between 10 and 90 °C with 5 min isothermal time at the extremes. Both heating and cooling cycles were repeated twice per measurement. An empty aluminum pan was used as a reference. The c_p values were estimated based on the third cycle in order to compare the materials after being exposed to the exact same thermal history.

The ***speed of sound*** (c) measurements were performed using a ResoScan acoustic interferometer from TF-instruments. The measuring equipment consisted of two identical resonator cavities with a length of 7 mm and a sampling volume of 180-200 µl. A detailed description of the method can be found in the study by Pfeiffer et al., [30]. An initialization was performed each time a new sample was introduced into the measuring tubes. To account for instrumental drift, one of the resonator cavities was filled with milliQ water (reference cell), while the other measurement tube was slowly filled with the sample [30,31]. The difference between the speed of sound of the sample and the reference was taken. Next, by adding this difference to the speed of sound of pure water, known from scientific literature [32], the speed of sound of the sample was calculated. A Peltier thermostat was used to control the temperature (±0.05 °C) and measurements were performed at 23 °C, 53 °C and 83 °C.

Surface tension (σ) measurements were performed using a Krüss K100C tensiometer, with a plate made of roughened platinum (Wilhelmy plate method) and in glass vessels of 100 ml (Krüss SV20, 70 mm internal diameter), filled with approximately 40 ml of solutions. Prior to the measurements of the samples, the surface tension of water was measured as a reference. The measurements were carried out at room temperature or the samples were preheated at the desired temperature on a heating plate before analysis and the temperature was recorded.

2.3. Experimental setups

The designed experimental setup allowed for online temperature recordings in combination with taking photos for the sonochemiluminescence (SCL) and the particle image velocimetry (PIV) experiments. The ultrasonic horn was inserted from the top of the reactor and placed in the desired insertion depth using a translation stage, as can be seen in Fig. 1, top. The electrical power input was adapted, for the horn to deliver the predefined tip axial movement. Depending on the performed experiments, the setup was modified as required. The dimensions of the reactor are presented in Table 1.

Some basic specifications of the ultrasonic horn follow in Table 2.

2.4. Calorimetric efficiency measurements

The electrical power input to the ultrasonic source was related to the power transferred to the medium with calorimetric experiments. Three thermocouples (K type) were placed inside the reactor at 0, 1.5 and 3.5 cm distance from the bottom, as close as possible to the wall of the vessel, and the average recorded value was calculated (Fig. 1, top). It is remarked here that placing a thermocouple very close to the horn should

Table 1
Dimensions of the reactor used for the experimental validation.

Diameter - D_R (mm)	Height - H_R (mm)	Bottom plate thickness (mm)	Jacket[1] thickness (mm)
52.6	80.9	7.3	16.7

Note[1] Cooling water circulated in the jacket via a thermostatic bath (Lauda Eco Silver RE630) to achieve the desired temperature.

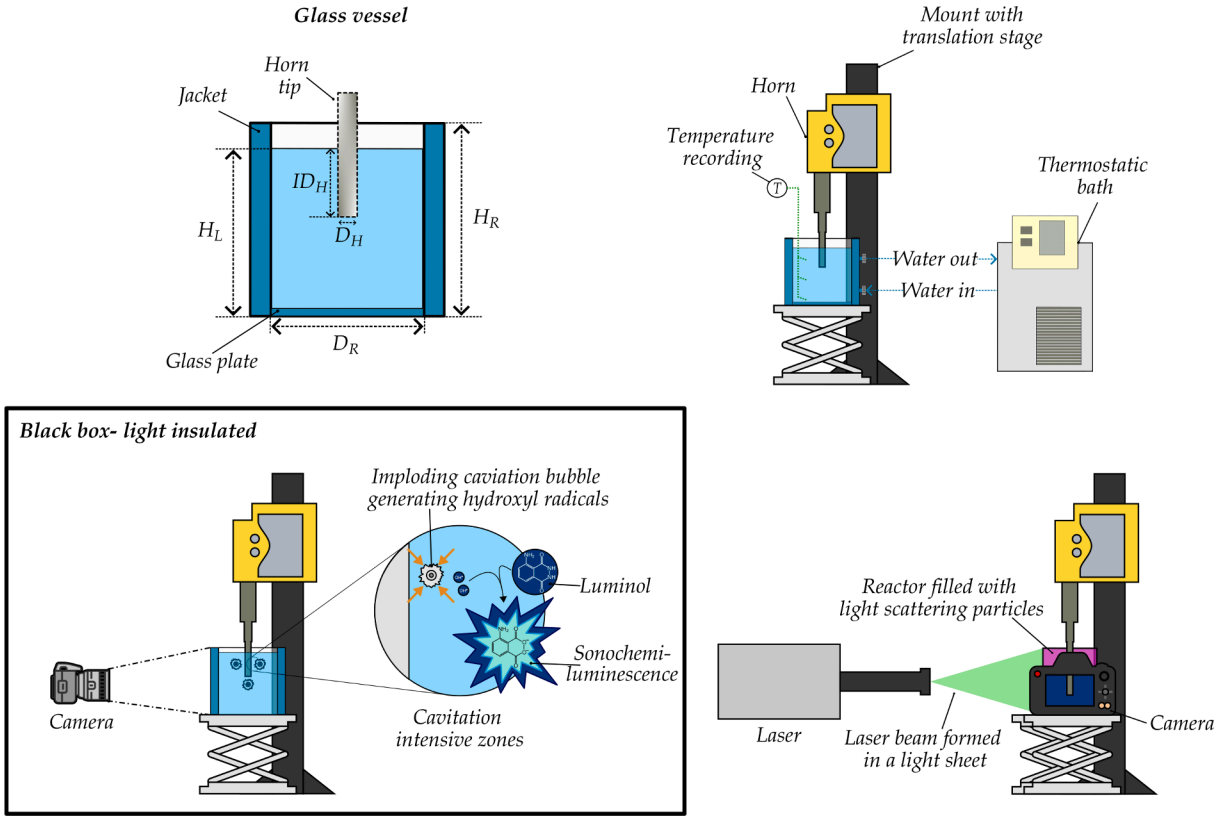

Fig. 1. Schematic representation of the experimental setup. Glass vessel - Key: D_R: reactor diameter, D_H: horn diameter, H_R: reactor height, H_L: liquid height, ID_H: horn insertion depth. Temperature recording (top right figure), SCL (bottom-left) and PIV (bottom-right) setups are also included in the figure.

Table 2
Overview of technical specifications of the ultrasound source used.

Type	Material	Tip diameter –D_H (mm)	Tip amplitude – r_{tip} (μm)		Maximum power (W)	Operating frequency (kHz)
			50%	100%		
Horn - Hielscher UP50H	Titanium	7	14.3	26.6	50	30

be avoided, as it will disturb wave propagation, create a passive nucleation center for cavitation, and eventually lead to damaging of the thermocouple itself due to collapse of cavitation bubbles on its surface. Further, the purpose of this study is to track the trend of the relative difference between electric and calorimetric power as function of viscosity in sonochemical experiments, rather than quantify the precise value of the calorimetric power itself. The actual electrical consumption of the US source was recorded with a voltameter. The temperature rise was recorded (Picolog 6 software) online while sonicating the liquid. During sonication the jacket of the reactor was filled with air in order to minimize heat losses. Using the temperature rise (dT/dt), the mass of the medium (m_{medium}) and the specific heat constant (c_P), the calorimetric power (P_{cal}) was calculated (Eq. (1)) and correlated to the electrical power (P_{el}) and calorimetric efficiency (η_{cal}) using Eq. (2). It should be noted that a cooling rate term (based on the cooling observed when sonication stops) could be included in Eq. (1). This term was considered negligible and was not included, based on the temperature recordings obtained for low and higher viscosity mixtures tested (Supporting Information, section A.2.). Specifically, when water was sonicated a linear temperature increase was recorded (Fig. 6S, left). When a higher viscosity sample was sonicated (40 wt% PEG8000) the inhomogeneity of the temperature distribution was quite high (Fig. 6S, right).

$$P_{cal} = m_{medium}.c_p.\frac{dT}{dt} \tag{1}$$

$$\eta_{cal} = \frac{P_{cal}}{P_{el}} \tag{2}$$

2.5. Sonochemiluminescence (SCL) & aluminum foil erosion (AFE)

In order to visualize the cavitationally active zones inside the reactor, the sonochemiluminescence (SCL) technique was used. This technique consists of sonication of aqueous solution of luminol (5-amino-2,3-dihydro-1,4-phthalazinedione) under alkaline conditions. Luminol readily reacts with the sonochemically produced hydroxyl radicals and the final product of this reaction (3-amino phthalate) emits blue light [1,22] which can be captured by a camera. In the current study, solutions containing 0.2 wt% luminol and 0.4 wt% NaOH were sonicated and images were captured inside a completely light insulated box (Fig. 1, bottom) using a Nikon Z6 II digital camera, with a NIKKOR optical lens (Z MC 50 mm f/2.8). The exposure time was 15 s, the focal ratio was 3.5 and the ISO setting was 25600. The obtained images allowed for qualitative and semi-quantitative characterisation of the cavitation zones inside the reactor. The relative SCL intensity was obtained by processing the images using a developed MATLAB script, with prior cropping and denoising. An image captured in silent conditions, was used as a blank and was subtracted from the images of the sonicated solutions in order to remove any background light. The blue light was used to compute the average light intensity, which was considered proportional to the intensity of cavitation events.

The aluminium foil erosion (AFE) is another visualization technique used, in order to verify the cavitation zones obtained with the SCL technique. Aluminum foil pieces were either wrapped around the horn or kept inside the liquid and positioned parallel to the direction of the horn inside the sonicated liquid [1]. The cavitational activity was measured qualitatively by the erosion caused on the foil surface, and the damaged spots were used as an indication of the cavitational active zones location.

2.6. Particle image velocimetry (PIV)

Particle image velocimetry (PIV) was employed to quantify the hydrodynamics of the system, using solid acrylic particles to visualise the streamlines. This technique is commonly used in fluid dynamics studies and is based on the determination of the particles displacement over time [1]. The particles were illuminated using a Litron S65 532 nm Nano PIV-S system equipped with two high intensity laser sources that generate pulses, one directly after the other. The laser pulses created a light sheet that illuminated a plane in the flow. Almost simultaneously with these pulses, two images separated by a small time delay (1 ms for water and the PEG-water mixtures, with exception of the PEG8000-water mixture for which 66.6 ms was used) were taken by a LaVision Imager LX 2 M synchronised high resolution camera equipped with an optical band-pass filter and Zeiss Discovery.V20 stereomicrosope, and in these consecutive frames the position of the particles was captured (Fig. 1, bottom). Images were captured over a short time span of few seconds to obtain a total of 180 frames per experiment. Based on the image pairs and known laser pulse delay, the particles displacement, velocity and circulation patterns could be determined using a cross-correlation algorithm (PIVlab) [1]. Processed data were extracted from the cross-correlation software package as text files and recompiled using a developed MATLAB script in order to obtain statistic results over all captured frames. Results are presented in terms of acoustic streaming velocity magnitude, normalised axial velocity and vector direction. The latter two provide more insight in the orientation of the individual vectors inside the flow field in addition to the mere magnitude of it.

3. Numerical section

3.1. Theoretical background on pressure acoustics

Assuming the case of linear wave propagation, the acoustic pressure inside a reactor can be obtained by solving the Helmholtz wave equation in the frequency domain:

$$\nabla^2 p_t + k_m^2 p_t = 0 \tag{3}$$

Where p_t is the total acoustic pressure and k_m is the modified complex wavenumber, accounting for damping. In the Commander and Prosperetti equation, considering acoustic attenuation due to a polydispersed population of cavitation bubbles [10,19] k_m is defined as following (Eq. (4)):

$$k_m^2 = \frac{\omega^2}{c^2} + 4\pi\omega^2 \int_0^\infty \frac{Rf(R,r)}{\omega_0^2 - \omega^2 + 2ib\omega} dR \tag{4}$$

With c the speed of sound of the medium, ω the angular frequency of the wave, ω_0 the resonance frequency of the bubbles, i the imaginary unit, b the damping factor, R the bubble equilibrium radius and $f(R,\boldsymbol{r})$ the number distribution function of the equilibrium radii.

A simplification of this equation (Eq. (4)) is Eq. (5) [10,19,22], for which a monodispersed bubble distribution of equal radius R_0 is assumed:

$$k_m^2 = \frac{\omega^2}{c^2}\left(1 + \frac{4\pi c^2 n_b R_0}{\omega_0^2 - \omega^2 + 2ib\omega}\right) \tag{5}$$

The number of bubbles per unit volume (n_b) included in the second term of Eq. (5) is related to the volume fraction of bubbles in the reactor (β) by the following correlation (Eq. (6)):

$$\beta = \frac{4\pi}{3} n_b R_0^3 \tag{6}$$

In the current study, the β factor was:

- Set equal to zero ($\beta = 0$), therefore neglecting the attenuation caused by bubbles in the medium
- Assumed constant ($\beta = constant$), considering homogeneous bubble distribution in the medium. A sweep was performed for the β over several decades based on literature values and using common R_0 values for water, as shown in Table 3.

When β was different from zero and freely chosen, the modified wavenumber was calculated (Eq. (5)) using the bubble resonance frequency (ω_0), the complex dimensionless parameter (Φ), the undisturbed pressure inside the bubble (p_0), the real dimensionless parameter (χ) and the damping factor (b), which were obtained via equations S3 to S8 (Table S9, Supporting Information). All the medium properties required to solve these equations were experimentally measured (density (ρ), speed of sound (c), surface tension density (σ) and dynamic shear viscosity (μ)). In addition, when monodispersed bubble distribution was assumed the properties of the gas inside the bubbles were required. The bubbles were assumed to be filled with air, hence the thermal diffusivity of the air inside the bubble (D) and the ratio of specific heats for air (γ) were defined as $D = 21.9{\cdot}10^{-6}\ m^2/s$ and $\gamma = 1.4$, respectively [35,36]. The equilibrium pressure in the liquid (p_∞) was also necessary and since the reactor was not pressurized $p_\infty = 1.01325{\cdot}10^5 Pa$.

To include the thermoviscous losses, the viscous fluid model was employed [37]. Therefore the speed of sound (c) was appended to a complex value (c_c) according to Eq. (7). In this approach bulk losses were accounted for, while the boundary layer losses were neglected which is a valid assumption at ultrasonic frequencies and lab (cm)-scale geometries [25].

$$c \rightarrow c_c = c\left(1 + \frac{i\omega b_{TV}}{\rho c^2}\right)^{\frac{1}{2}} \tag{7}$$

The damping parameter of the thermoviscous model (b_{TV}) could be calculated using Eq. (8):

$$b_{TV} = \left(\frac{4}{3}\mu + \mu_B\right) \tag{8}$$

The bulk viscosity (μ_B) is not easily measured, therefore it was assumed equal to the dynamic shear viscosity (μ), which is a reasonable approximation since the bulk viscosity is often in the same order of magnitude as the shear viscosity [25,37,38].

The combination of the cavitation and thermoviscous based attenuation (Eq. (5) and Eq. (7)) resulted in the following expression for the complex, extended wavenumber:

$$k_{m\_TV}^2 = \frac{\omega^2}{c_c^2} + \frac{4\pi\omega^2 n_b R_0}{\omega_0^2 - \omega^2 + 2ib\omega} \tag{9}$$

In the first part of this equation (Eq. (9)) the thermoviscous damping parameter was superimposed to the Commander-Prosperetti equation.

3.2. Threshold pressure estimation for increasing viscosity mixtures

For all increasing viscosity mixtures, the minimum pressure amplitude for transient cavitation of bubbles was determined by modelling the dynamics of the bubbles. An approach similar to Rossi et al. [22] was taken. Specifically, it was assumed that when the velocity of the bubble wall reduction (dR/dt) is greater than the sound velocity at the collapse time, then transient cavitation occurs. The Mach number ($M = \dot{R}/c$) was estimated, by solving the Keller-Miksis equation (Eq. (10)) which was used to compute radial oscillations for different initial bubble radii and acoustic pressure amplitudes (p) [21,22,33].

$$\rho\left[\left(1 - \frac{\dot{R}}{c}\right)R\ddot{R} + \frac{3}{2}\dot{R}^2\left(1 - \frac{\dot{R}}{3c}\right)\right] = \left(1 + \frac{\dot{R}}{c} + \frac{R}{c}\frac{d}{dt}\right)\left(p_g - \frac{2\sigma}{R} - \frac{4\mu\dot{R}}{R} - p\right) \tag{10}$$

With R representing the instantaneous bubble radius at time t, overdots indicating differentiation with respect to time and p being the pressure at the center of the sonicated bubble. In order to solve the bubble dynamics, the time dependent bubble gas pressure (p_g) should be known [33]. Therefore, adiabatic bubble expansions and compression states were assumed and the polytropic ideal gas (Eq. (11)) law were simultaneously solved [39], with $\gamma = 1.4$ and p_{g0} the Laplacian gas pressure inside a quiescent bubble.

$$p_g \cdot R^{3\gamma} = p_{g0} \cdot R_0^{3\gamma} \tag{11}$$

3.3. Model setup

A FEM simulation is utilised to simulate the setup in COMSOL Multiphysics 6.0, using the Pressure Acoustics module in the frequency domain and employing a stationary solver. This means that the acoustic pressure was assumed to oscillate linearly at the angular driving frequency ω.

3.4. Reactor geometry, numerical mesh and boundary conditions

A schematic representation of the geometry and the mesh used to model the setup is presented in Fig. 2.

A two-dimensional axisymmetric geometry was used aiming to limit the computational efforts. A free triangular unstructured mesh was chosen as computational grid. A COMSOL physics defined mesh was employed, with a predefined amount of mesh elements per wavelength (12867 number of elements and 2793 mm^2 total mesh area). To avoid numerical pollution, the number of mesh elements per wavelength satisfied the $k{\cdot}h << 1$ criterion, with h the average size of the mesh elements and k the wavenumber [7,10,22,40].

The used boundary conditions for non-vibrating surfaces included:

- **Sound soft BC**, for pressure release near a wall ($p_t = 0$) [37]. This condition corresponds to a phase shift of the pressure wave of 180° upon perfect reflection [7,9,10,15].

Table 3
Overview of the investigated volume fractions and equilibrium bubble radii.

Attenuation parameter	Value								
R_0 (μm)	1	3	10	30					
Reference	[33]	[11,23]	[11]	[22], this work[2]					
β [1]	0	$4{\cdot}10^{-7}$	$4{\cdot}10^{-6}$	$4{\cdot}10^{-5}$	$9{\cdot}10^{-5}$	$4{\cdot}10^{-4}$	$9{\cdot}10^{-4}$	$4{\cdot}10^{-3}$	$9{\cdot}10^{-3}$
Reference	[7,10]	[23]	[23], this work[2]	[8,11]	[8,11]	[10,22,34]	[10,34]	[8,10,34]	[8,10,34]

Note[1] $\beta = 0$ corresponds to neglecting cavitation based attenuation, $\beta = 0.1$ is the maximum limit for achieving realistic damping values according to [10,34].
Note[2] Parameters used for the results presented in the current paper.

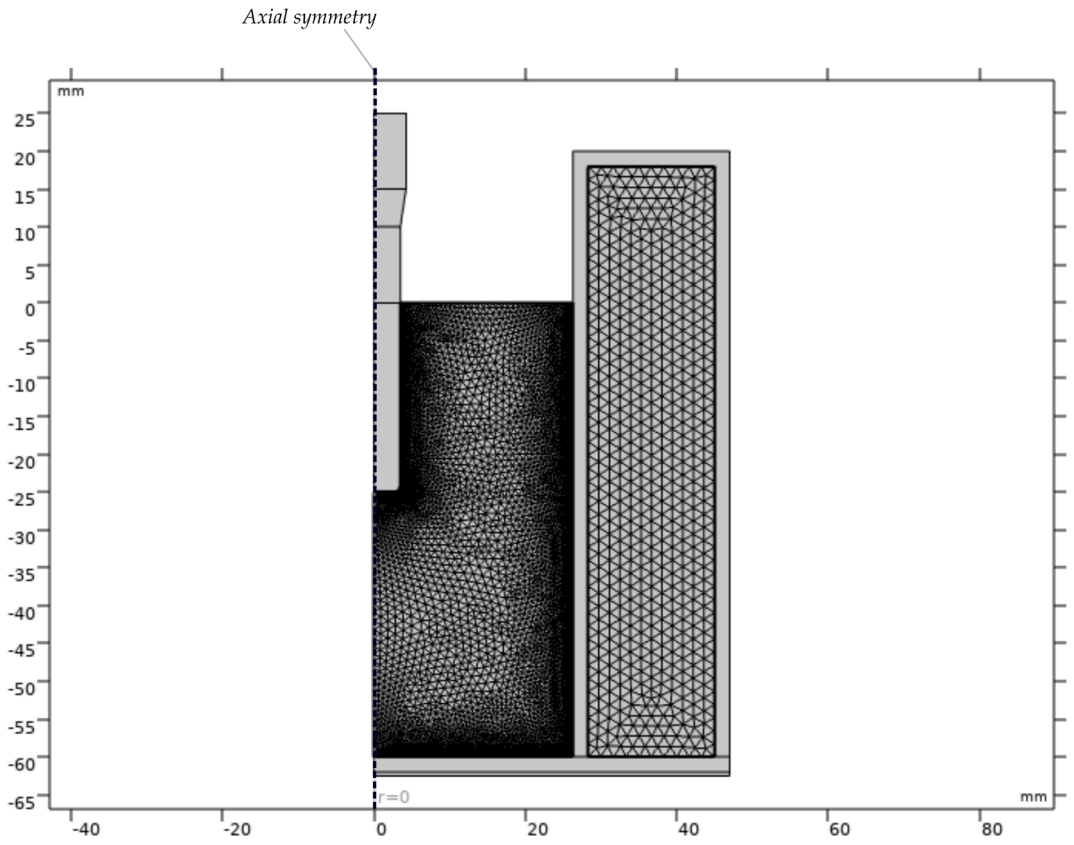

Fig. 2. Geometry setup of the ultrasonic horn reactor in 2D.

- **Sound hard BC,** meaning that the normal acceleration and velocity were zero ($\alpha_n = 0$) [10,37]. This condition assumes the incident and reflected pressure waves to be in phase.

For the vibrating surfaces (horn tip and horn walls) pressure or normal displacement BC were tested:

- **Pressure BC,** for which a fixed pressure amplitude was imposed ($p_t = p_{t0}$) [37]. The plane wave formulation was used to relate the pressure amplitude at this boundary to the power input to the ultrasonic actuator [10,22,23]:

$$p_{t0} = \sqrt{\frac{2\rho c P_{US}}{S}} \tag{12}$$

With ρ the real medium density, c the medium speed of sound and S the irradiating surface area. P_{US} the ultrasonic power transferred to the liquid, which was assumed equal to the calorimetric power (P_{cal}).

- **Normal displacement BC** was applied using Eq. (13) to obtain the normal acceleration a_n, using the amplitude of the vibrating surface (r_{tip}), vibrating at frequency f (assuming sinusoidal oscillations):

$$a_n = 4\pi^2 f^2 r_{tip} \tag{13}$$

An overview of the mathematical equations for the boundary conditions used for vibrating and non-vibrating surfaces is provided in Table S10 (Supporting Information). Two versions of the numerical model were prepared, with main difference the BC implemented for the US horn. For the first version (named "Pressure BC" model hereafter), pressure BC was applied at the horn tip and sound hard BC at the horn wall. For the second version of the model (named "Displacement BC" model hereafter), normal displacement was applied for both the tip and the shaft of the horn. The non-vibrating boundaries, such as the liquid-air interface and the reactor walls were modelled as sound soft or sound hard. The choice between sound soft and sound hard BC can be based on the specific acoustic impedance of the boundary material (Z_i). Looking at the sound impedance equation in Table S10, when $Z_i \approx 0$ sound soft BC should be applied and when $Z_i \approx \infty$ sound hard BC was the correct choice. Acoustic impedance values from the literature (Table S11, Supporting Information) showed that the water- air interface can be considered sound soft BC, while the reactor and horn walls are closer to sound hard BC. Nevertheless, reactor walls were also modelled as sound soft ($p_t = 0$, Table S10), similarly to other works reported in the literature [7,22]. This assumption is only valid if the wall thickness is negligible when compared to the ultrasonic wavelength [7,9,22] which was the case for the applied frequency in the current paper (for 30 kHz, the wavelength is 4.97 cm for water as the medium, the jacket thickness is 1.67 cm and the bottom plate thickness is 0.73 cm).

A summary of the implemented boundary conditions for the two model versions is presented in Fig. 3.

4. Results and discussion

4.1. Properties of the investigated mixtures

An overview of the measured properties of the selected PEG-water mixtures at 23 °C can be found below in Table 4.

The density (ρ) of the mixtures showed a decreasing trend with increasing temperature, while higher values were obtained for higher glycol concentrations (Figure S1). The data was correlated using 1st or 2nd order polynomials and showed satisfactory fit over the applied range of temperatures for all measured samples with the lowest R^2 equal to 0.961 (Table S1). The highest viscosity (μ) of the PEG water mixtures was almost 760 times higher than the viscosity of water (712.5 mPas for the 40 wt% PEG20000 sample). The temperature dependency of the data was obtained by an Arrhenius fitting (Eq. S1) with good agreement for all the samples (Table S2). Regarding the obtained sound velocity of

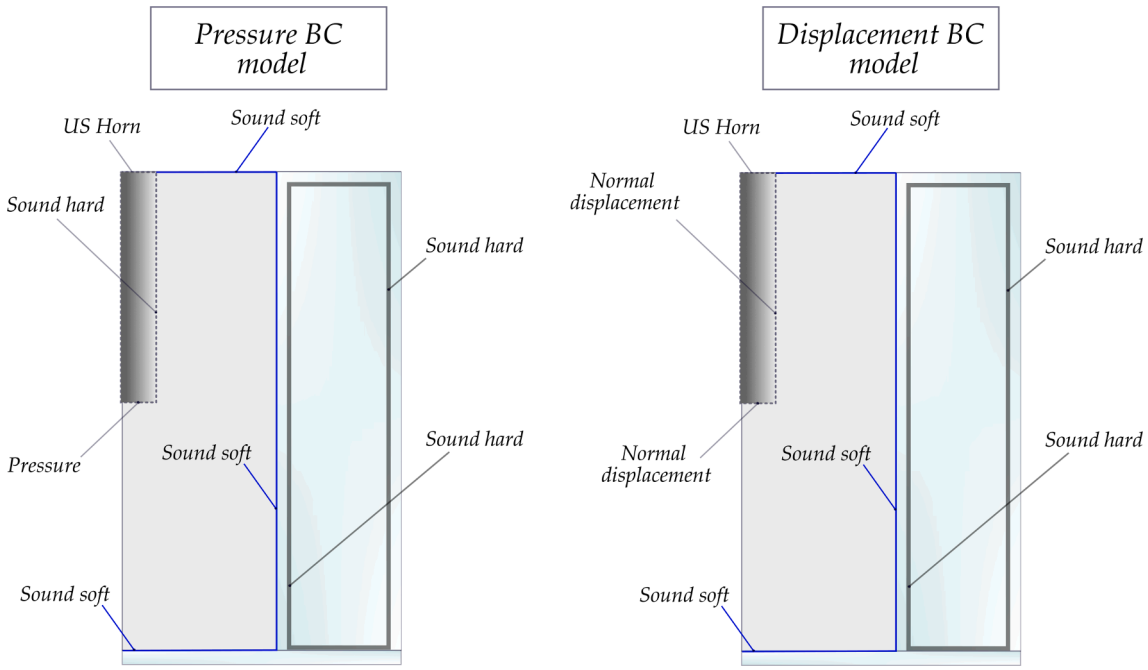

Fig. 3. Simplified scheme for the boundary conditions implemented for the developed models using a horn as the US source.

Table 4
Overview of experimentally measured properties for various mixtures and pure compounds at 23 °C.

Sample	ρ (g/cm^3)	μ (mPa s)	c_p (J/g °C)	c (m/s)	σ (mN/m)
40 wt% PEG20000	1.069	712.5	2.570	1720	53.6
40 wt% PEG8000	1.069	123.2	3.310	1731	54.4
PEG400	1.124	103.8	2.087	1599	46.5
90 wt% PEG400	1.122	89.6	2.427	1657	47.7
40 wt% PEG4000	1.069	45.8	3.413	1727	57.2
70 wt% PEG400	1.110	36.9	2.679[1]	1748	51.0
40 wt% PEG2000	1.069	22.2	3.691	1728	56.7
10 wt% PEG20000	1.010	7.5	4.021	1546	58.9
40 wt% PEG400	1.064	6.4	3.511	1718	52.5
10 wt% PEG8000	1.014	5.1	4.026	1549	57.7
10 wt% PEG4000	1.018	2.6	4.020	1551	57.9
10 wt% PEG2000	1.014	2.0	4.265	1550	55.1
10 wt% PEG400	1.014	1.3	3.787	1507	57.3
Water	0.998	0.9	4.060[2]	1491	71.9[2]

Note[1] The c_P value for this mixture was obtained using a linear mixing rule.
Note[2] For water the data from COMSOL were used for all properties, with exception of the c_p and the σ values, that were obtained experimentally.

the PEG400-water mixtures (c), a non-linear dependency on the water (or PEG400) concentration was obtained (Figure S5) which is indicative of the non-ideal nature of the mixtures. The existence of a maximum for the speed of sound is correlated with a minimum of the adiabatic compressibility [31,38,41] and of the excess molar volume [31]. The addition of water resulted in the formation of hydrogen bonds with the polymer, thereby increasing the mixture volume [31]. All data obtained were linearly plotted in the applied temperature range with good fitting, exception were all the 10 wt% mixtures for which linear fitting was not satisfactory (Table S4). At this water concentration the speed of sound values follow the non-linear behavior as indicated by the model of Del Grosso and Mader (Figure S4). The data for the surface tension can be found in Table S5. The created database for all properties, their temperature dependency and validation with available literature data can be found in the Supporting Information (Section A1.1 to A1.5).

4.2. Impact of viscosity increase on calorimetric power and SCL emission

4.2.1. Calorimetric power results

Samples prepared with the same PEG content (40 wt%) were selected for the calorimetric power study. Specifically, the viscosity of these samples covered the range of three orders of magnitude, with 40 wt% PEG400 at ≈6 mPas, 40 wt% PEG2000 at ≈22 mPas, 40 wt% PEG4000 ≈46 mPas, 40 wt% PEG 8000 at ≈123 mPas and 40 wt% PEG 20000 at ≈713 mPas. The density and speed of sound of these samples remained almost identical (Table 4). Water was also tested (≈1 mPas) for reference. The impact of viscosity on the calorimetric (P_{cal}) and electrical power (P_{el}) input can be seen in Fig. 4.

As a first observation, both P_{cal} and P_{el} increased with viscosity increase up to ≈46 mPas for both horn insertion depths tested (25 and 35 mm). At ≈123 mPas both powers decreased sharply, and for the highest viscosity tested (≈713 mPas) the values reduced to up to 40% of the P_{cal} of water (7.1 W for 40 wt% PEG20000 and 17.9 W for water, at 35 mm horn insertion depth). The average recorded dT increased from ≈3 to 7 °C (for 0.9 to 46 mPas), remained almost unchanged (≈7 °C for 46 and 123 mPas samples) and dropped to ≈3 °C for the sample with the highest viscosity (712 mPas). Another observation was related to the temperature gradient recorded in the vessel depending on the solution tested. For the samples with viscosity up to ≈46 mPas the measurements of the three thermocouples were in good agreement (maximum temperature difference of 3.1 °C between the three sensors). For the samples with the highest viscosities (≈123 and 713 mPas) the deviation of the temperature recorded by the three sensors reached a temperature difference of 9.1 °C (Figure S6, Supporting Information). The ultrasonic horn device used in this paper is designed to deliver a specified and continuous amplitude at the tip [42], therefore the initial increasing electrical power trend (samples with viscosity up to 46 mPas) can be explained by the viscosity or fluid resistance build up. It could also be assumed that a considerable part of the energy input results into direct heating via viscous losses at the horn tip, instead of being consumed by bubbles oscillations.

For samples with the highest flow resistance (viscosity of ≈123 and 712 mPas), the horn was found to be pulsating - even though it was set at continuous operation. As a result, a decrease in the electrical power was observed, correlated to the internal modulation of the device, which

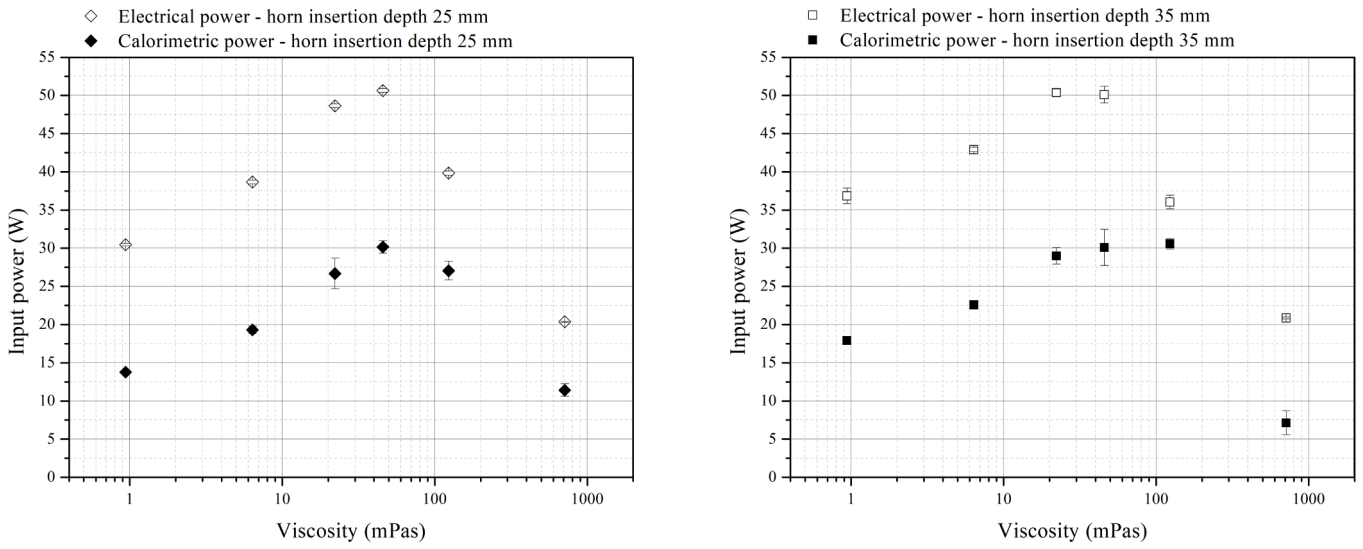

Fig. 4. Calorimetric and electrical powers for liquid height of 60 mm, input power of 100%, and horn insertion depth of 25 mm (left) or 35 mm (right). Standard deviation values based on three replicates are included in the graphs.

fluctuated between the on and off operating mode. The calorimetric power, strongly correlated to the electrical power (Table S7, Supporting Information), followed the same trends: increasing for samples with viscosity up to 46 mPas, followed by a decrease for the highest viscosity samples. An additional reasoning for the drop of P_{cal} was the poor heat diffusion within the liquid. Specifically, the temperature increase for the liquid layers located next to the horn tip or horn walls was high, in contrast to the temperature recorded for the layers closer to the bottom of the vessel or the liquid–air interface.

4.2.2. Sonochemiluminescence (SCL) and luminol intensity results

Similarly to the calorimetric power input, the SCL experiments were performed for water and 40 wt% PEG solutions. Luminol and NaOH concentrations were kept equal for all the samples tested. Two horn insertion depths ($ID_H = 25$ and 35 mm) were applied and the obtained photos can be seen in Fig. 5.

Two cavitational active zones were observed: one directly under the horn tip and one around the immersed horn shaft. The zones were visually larger for the deepest horn insertion depth ($ID_H = 35$ mm, Fig. 5, top). In general, non–uniform SCL distribution is expected as liquid sonication in a small closed vessel creates a resonant acoustic field that is dynamically disturbed by several effects that are inherently non-uniform or not completely symmetrical, such as the trajectory of horn vibration in the liquid, acoustic streaming, main flow patterns, bubble distribution, local hot spots and minor local defects (pits) on the horn surface. When comparing only the PEG–water mixture photos, brighter and larger zones were observed for the lower viscosity samples, with a qualitative maximum for the lowest viscosity sample of 6.4 mPas (or 40 wt% PEG400). With increasing viscosity, the light intensity decreased and reached a minimum for the sample of 712.5 mPas (or 40 wt% PEG20000) for which only a weak light zone appeared directly at the horn tip for both insertion depths tested.

The light intensity for sonication of water was also among the highest recorded, but it could not be directly compared to the PEG-water samples due to the difference in the mixtures composition. Specifically, the presence of PEG in water might interfere with the total light emission, making a proper quantitative comparison difficult. The SCL photos from Fig. 5 were post-processed with a custom developed image analysis code and the relative SCL intensity was obtained based on the integrated blue light intensity of each photo. The results, presented in Fig. 6 confirmed quantitatively the aforementioned observations related to the impact of viscosity rise in a decrease of the total SCL activity. The relative SCL intensity of water was plotted as reference for both horn insertion depths tested. The results from the RGB spectrum (red, green and blue channels) analysis of the images can be found in Figure S7.

In order to clarify if the second noticed zone along the horn body was

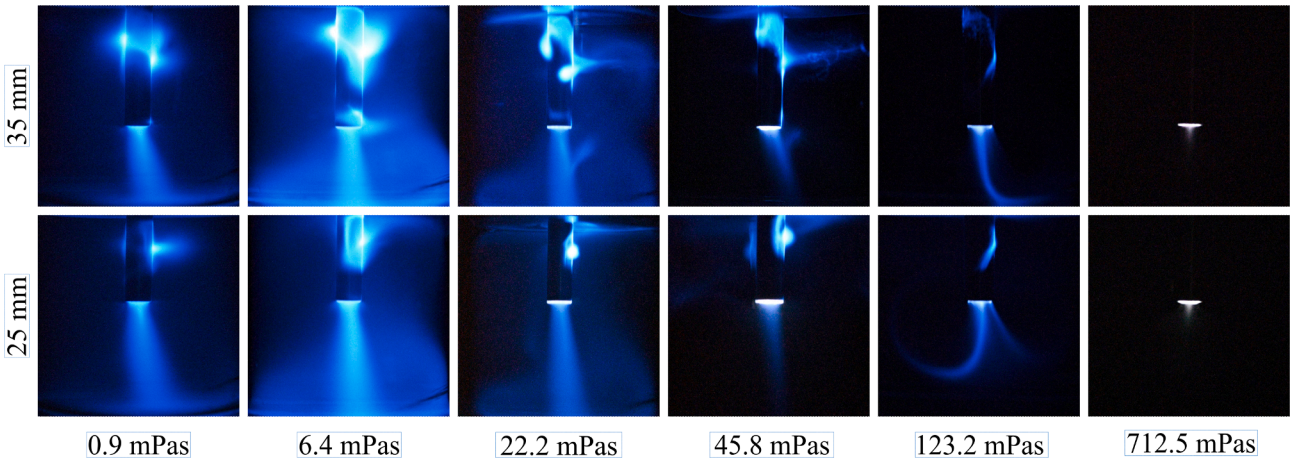

Fig. 5. SCL images for increasing viscosity solutions, liquid level of 60 mm, sonication power of 100% at horn insertion depth of 35 mm (top) and 25 mm (bottom).

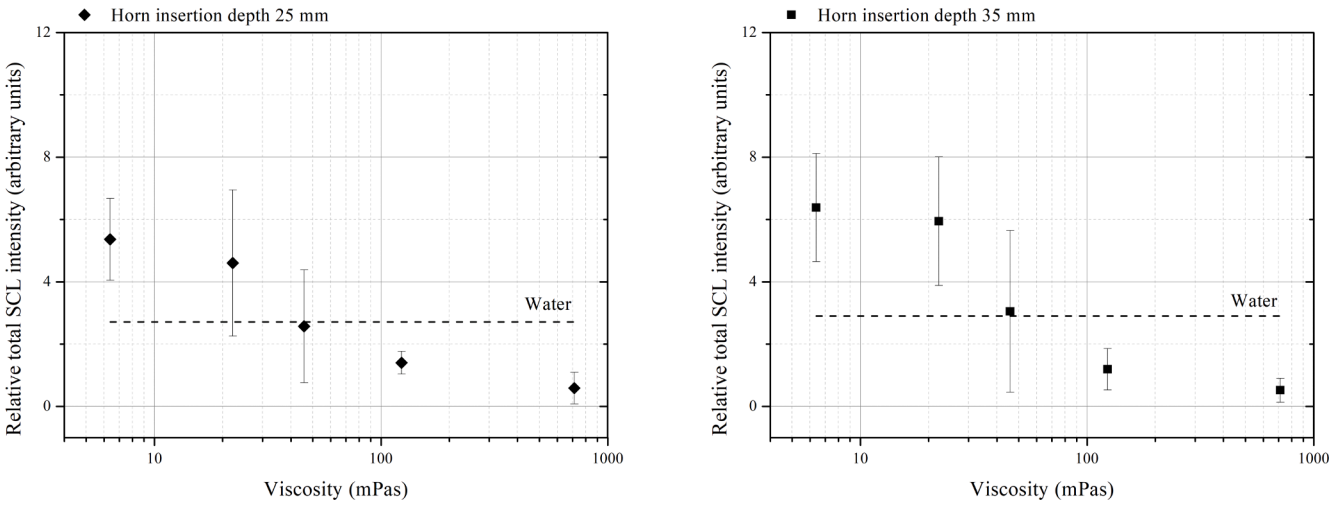

Fig. 6. Relative total SCL intensity for increasing viscosity mixtures, liquid level of 60 mm, sonication power of 100% at horn insertion depth of 25 mm (left) and 35 mm (right). The SCL intensity for water is plotted as reference in both figures. Error bars represent the standard deviation of three repetitions per sample.

a result of light reflections at the bottom of the vessel or a cavitationally active zone, the aluminum foil technique was employed and the results can be seen in Figure S8. The aluminum erosion patterns observed confirmed that the two zones were the result of cavitation activity. As an additional test, the horn was immersed in a vessel of 1 L in order to minimize possible acoustic reflections caused by the bottom or side walls of the vessel, as was mentioned in the literature [43,44]. The presence of the zones remained unchanged as can be seen in Figure S9. It was therefore confirmed that the presence of the second zone along the shaft of the horn was related to radial movement of the horn, which expands and contracts while sonicating a solution. Louisnard and Garcia-Vargas attributed this to the "flow of acoustic energy through the lateral boundaries of the transducer" [21].

Finally, by combining the results obtained in the calorimetric experiments (Fig. 4) and the SCL images (Fig. 5), the substantial role of both viscosity and surface tension for the occurring local cavitation events can be discussed. Specifically, the modification of the surface tension of the sonicated solution can strongly affect the potency of bubbles collapse, with larger bubble radii and higher pressure required for larger surface tension samples [45]. This is observed in Fig. 5, when comparing the brightness of the photographs of water (0.9 mPas) and 40 wt% PEG400 solution (6.4 mPas), corresponding to mixtures with surface tension of 71.9 and 52.5 mN/m, respectively (approximately 30% surface tension decrease, Table 4). At the same time, the role of viscosity in the transition between violent and smoother collapse is not straightforward, however it has been reported that the optimum region for powerful bubble collapse lays in the viscosity range of up to ≈ 40 mPas [45]. Therefore, the observed transition of P_{cal}/P_{el} in this region (Fig. 4) could also be correlated to switching to a different bubble oscillation/ collapse regime.

4.3. Impact of higher viscosity in particle velocities and their circulation pattern

A representative subset of the PEG-water solutions (with viscosity of 0.9, 22.2, 45.8 and 123.2 mPas) was used to study the impact of viscosity increase on the acoustic streaming behavior in the reactor. The solutions were selected based on preliminary experiments performed. Acoustic streaming is a result of the heterogeneous acoustic pressure distribution inside the reactor, generating a non–zero convective acceleration of (first order) acoustic perturbations that act upon all fluid parcels inside the sonicated domain [46]. Given the nature of the streaming profiles and the camera view field, two regions of interest were identified as shown in Fig. 7. The first region concerned the axial zone directly below the horn tip, whereas the second focused on the radial zone left of the horn.

Results of the image velocimetry in terms of streaming velocity vectors are shown in Fig. 8 (Axial region top, Radial region bottom) for the different mixtures and for two insertion depths tested (25 and 35 mm). Congruent with prior work in the literature, a strong downward jet is observed below the sonotrode tip [47–49]. As the viscosity of the mixtures increased, the flow profiles became increasingly laminar. Moreover, the velocity magnitude decreased from approximately 0.3 m/s when water was sonicated to approximately 0.1 m/s for the 40 wt% PEG8000 sample. For reference, streaming velocities of approximately 0.4 m/s were obtained when water was sonicated at 20 kHz in the work of Yamamoto et al., [49]. An increase in the velocity magnitude was observed when comparing water to the PEG-water samples (0.9 to 22.2 mPas) (Figure S10 and S11, Supporting Information). This could be attributed to the impact of PEG addition to the mixtures composition, similarly to what was observed in the SCL results. When comparing only the PEG-water samples (22.2, 45.8 and 123.2 mPas samples) the decreasing trend in velocity magnitude was confirmed, both for 100 and 50% sonication power (Figures S10 to S13, Supporting Information). The Navier-Stokes equation dictates lower velocities for more viscous fluids for a certain, but fixed volumetric driving force. The volumetric driving force itself is in fact also not constant, but increases with increasing viscosities as a result of increased

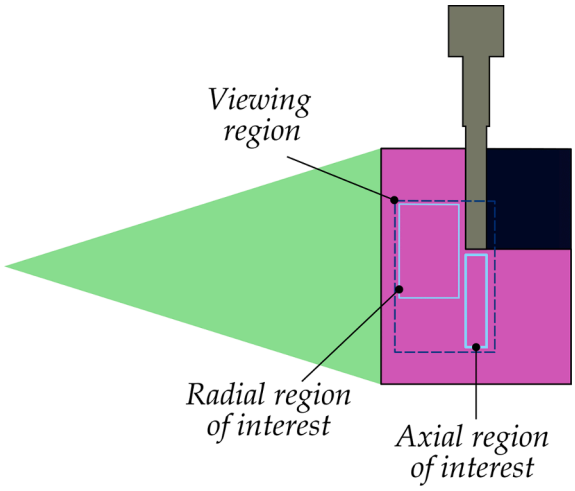

Fig. 7. PIV viewing, axial and radial regions of interest.

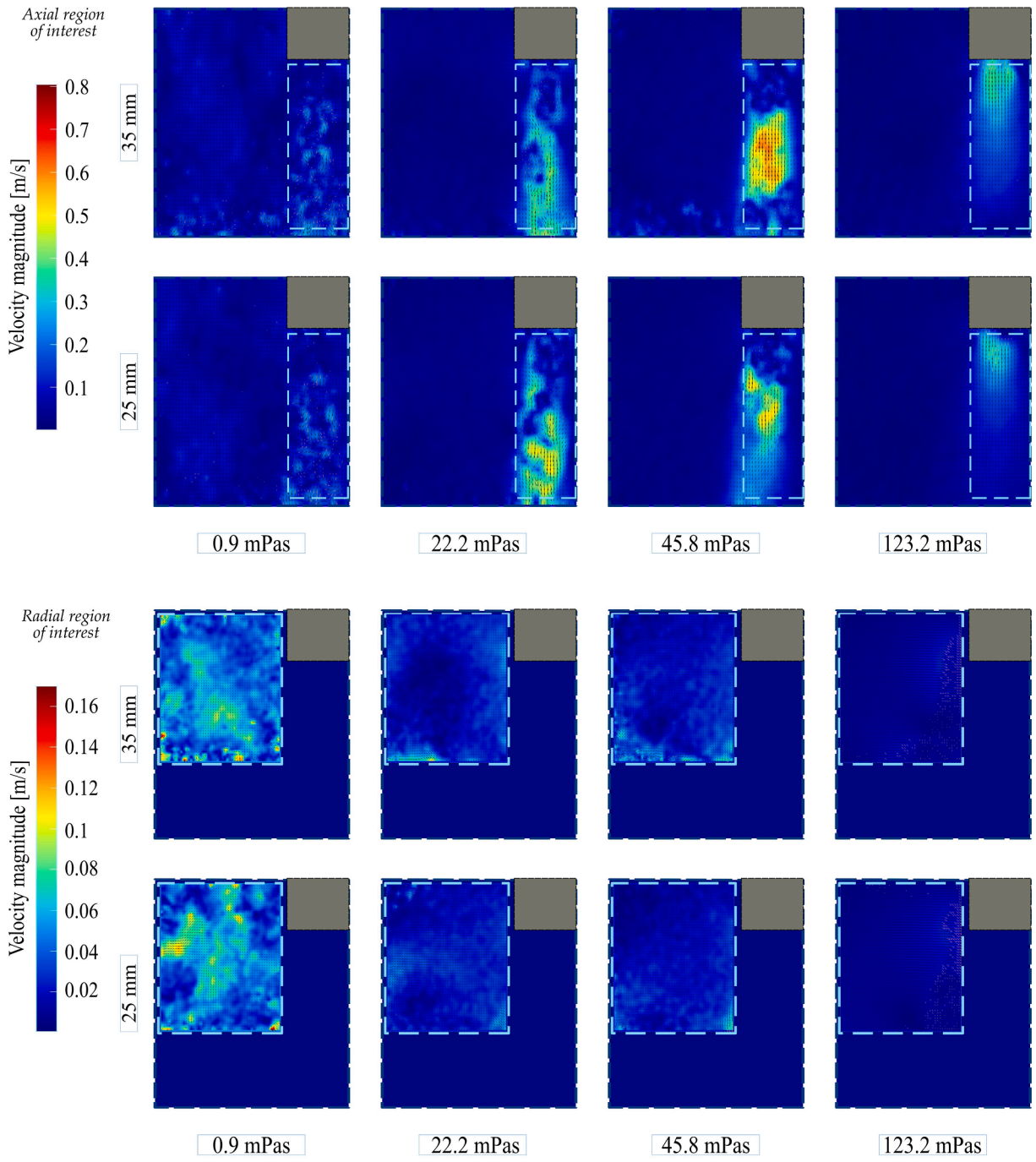

Fig. 8. Acoustic streaming velocity vectors for increasing viscosity mixtures, liquid level of 60 mm, sonication power of 100%, horn insertion depth of 35 mm or 25 mm. On the top of the figure the focus is on the axial region of interest and on the bottom on the radial region of interest as indicated inside the figure. Vector scaling calibrated and normalized across the datasets.

viscous dissipation of the sound wave, creating steeper pressure amplitude gradients [50,51]. It should be noted that the driving force is no direct function of the acoustic pressure magnitude (which does not necessarily decrease as viscosity increases, given that bubble oscillations in cavitating liquids can become so damped that the radial velocity decreases, reducing the power dissipated by the bubble and thereby locally increasing the acoustic pressure [29,48]) but rather the gradient in acoustic pressure.

Characteristic vortices were observed at the side walls of the horn. For lower viscosities, the vortices were more difficult to recognize due to the increased turbulence associated with these mixtures. The nature of this turbulence could be directly attributed to the effect of viscosity, though it is possible that cavitational activity, which is more spatially distributed at lower viscosities, provides an additional contribution to the local Kolmogorov's scale eddies. Another observation was related to the velocity magnitude of the fluid parcels contained in the vortex next to the horn walls, which was much smaller (approximately 5 times) compared to the downward jet for all mixtures tested as seen in Fig. 8. The recirculation velocity of particles was found 3-5 times lower than the axial velocity in the literature [52], which comes in good agreement.

Statistics of the velocity magnitude, normalized velocity and vector directions, representative for the circulation pattern in the axial and radial zone respectively, are shown in Figures S10 to S19 (Supporting Information, section A.4.). by means of a histogram plot. These graphs

incorporate all images captured during the total recording time and provided a more holistic approach to interpretation of the streaming behavior across space and time. Neither of these properties were normally distributed, but rather approached a Poisson distribution (as in, the probability of certain velocity magnitude or vorticity occurring at a certain time instance somewhere in the region of interest has a constant mean rate and occurs independently of the previous instance). The normalized axial velocity and vectors direction (Figures S14 to S19) provide insights in the orientation of the vectors flow field with respect to the horizontal plane. For strictly jetting flows, the normalized axial velocity must be equal to one at all locations (corresponding to an angular polar plot of the vectors direction indicating only 0° or 180°). For strictly rotational vortices, the angular polar plot of the vector directions would be a perfect circle, indicating all orientations to be equally present.

4.4. Impact of viscosity increase on numerical results: Cavitation threshold pressure and numerical simulations

4.4.1. Cavitation threshold determination

For higher liquid viscosities an increase in the threshold pressure (i.e. the minimum pressure required for cavitation to occur) was remarked as presented in Fig. 9.

For initial bubble radius of 1 μm, it was noted that the threshold pressure of pure water ($0.163 \cdot 10^6$ Pa) exceeded the mixture of 6.4 mPas ($0.154 \cdot 10^6$ Pa). This can be attributed to the higher surface tension of water (71.9 compared to 52.5 mN/m) and the dominant surface effects at small radii [53]. The above values for the threshold pressure were used to compute the simulations for each of the mixtures prepared.

4.4.2. Pressure BC model results

The pressure BC model (detailed results in Section C.1, Supporting Information) did not reproduce well the experimental measurements. Therefore, this model was considered inadequate and the displacement BC model was developed (4.4.3).

4.4.3. Displacement BC model results

For the displacement BC model, the observed radial horn movements as explained in Section 4.2.2 were taken into consideration. The boundary conditions were kept similar to the pressure BC model, with exception the BC of the horn tip and the horn walls, for which normal displacement BC was applied (Fig. 3). The radial displacement was assumed constant and equal to 10% of the axial horn displacement, in order to achieve the best correlation to experimental data. In the work of Louisnard and Garcia-Vargas [21] a similar experimental configuration

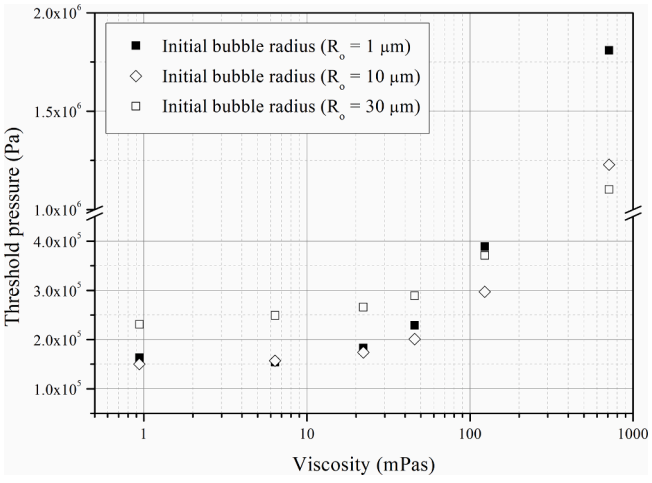

Fig. 9. Threshold pressure estimation for increasing viscosity mixtures and three different initial bubble radii (1, 10, 30 μm).

was modeled, and for horn immersion depth higher than 30 mm their model predicted ≈12% of energy input originating from the lateral walls of the horn. The obtained simulation results can be seen in Fig. 10. The zones where the threshold pressure was exceeded are marked with white lines.

By comparing the numerical simulation results of Fig. 10 to the SCL photos of Fig. 5 some observations can be made. Firstly, the model was able to qualitatively predict well the location of the two cavitation zones. For all the mixtures, two high pressure zones were predicted: one directly at the tip of the horn and one along the body of the horn. Exception was the highest viscosity mixture (712.5 mPas), for which the cavitationally active zone was limited to one directly at the horn tip area, which was correctly predicted by the model. Secondly, the predicted zones location remained correct for a decrease in the horn insertion depth from 35 to 25 mm. Finally, the impact of viscosity increase, which is related to the viscous dissipation increase [29], was also captured, and diminished cavitation zones were obtained.

On the downside, two major points can be mentioned. Firstly, the collapse intensity is not included in the numerical model and it was therefore not properly captured. The model prediction showed larger and more intensive zones for water compared to the 6.4 and 22.2 mPas (40 wt% PEG400 and 40 wt% PEG2000) samples. The SCL results showed the opposite trend, namely the zones were larger and more intense for the 6.4 and 22.2 mPas solutions (Fig. 5). Higher light intensity can be correlated to increased concentration of ·*OH* radicals that reacted with the luminol of the solution, indicating higher cavitation activity [43]. An experimental investigation by Young coincided with this finding, and reported higher sonoluminescence (SL) activity for increasing viscosity glycerin-water mixtures [54]. In addition, Yasui et al., attributed the higher SL light emissions to more powerful bubble collapse in increased viscosity mixtures [55]. It should be noted that in both works, SL instead of SCL was investigated. Nevertheless, both methods are related to the conditions upon bubble collapse, with higher temperature usually required for SL bubble collapse [56]. Secondly, the proportion between the area and the intensity of the two predicted zones (at the horn tip vs horn body) was not correctly anticipated by the model. For example, for $ID_H = 35$ mm the model predicted higher intensity at the tip of the horn that should correspond to higher light emission in the SCL photos, which was not the case. This could be attributed to the under prediction of attenuation per wavelength associated with the assumption of linear bubble oscillations [21], misleading to larger zones of increased acoustic pressure. The total relative cavitation zone size, being the ratio of the cavitation cells over the total mesh cells per mixture, was extracted from the COMSOL simulations and the obtained results can be seen in Fig. 11.

The relative cavitation zone size predicted for water was the highest, 26.2 and 44.2% for horn insertion depth of 25 and 35 mm respectively (Fig. 11). As viscosity increased, the cavitation zone size predicted reduced. For samples with viscosity from 6.4 to 123.2 mPas, the relative cavitation zone size estimated by the model was 30-50% of the zone size predicted for water. At the extreme viscosity of 712.5 mPas, the cavitation zone size predicted by the model was 90-95% lower than the estimation for water, with 1.3% for $ID_H = 25$ mm and 5.6% for $ID_H = 35$ mm. In general, higher zone size was foreseen for deeper insertion depth which would be expected due to the contribution of the zone at the body of the horn.

5. Conclusions and future perspectives

In this paper the impact of the medium viscosity on the ultrasound field is explored both experimentally and numerically. Firstly, PEG-water solutions were prepared and characterized in terms of their physicochemical properties. The viscosity of the samples increases to 712.5 mPas when PEG20000 is used as the diol. Secondly, the solutions were sonicated using a 30 kHz horn, operating at 100% amplitude and inserted at two different depths.

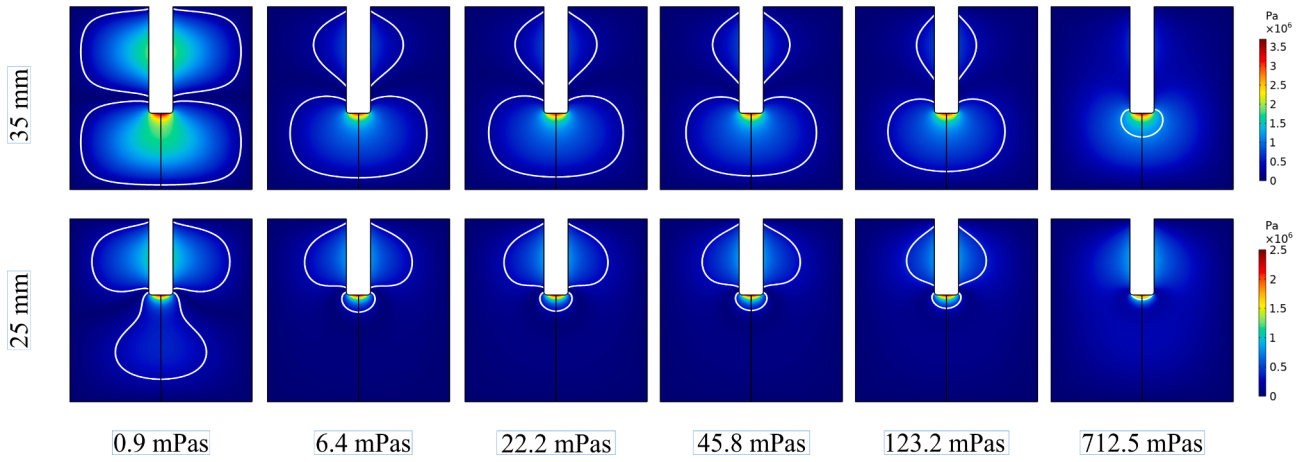

Fig. 10. Displacement BC model results for increasing viscosity solutions, liquid level of 60 mm, sonication power of 100% at horn insertion depth of 35 mm (top) and 25 mm (bottom).$R_0 = 30\ \mu$m and $\beta = 4{\cdot}10^{-6}$. The white lines in the model photos mark the cavitation zones where the predicted acoustic pressure exceeded the chosen threshold value.

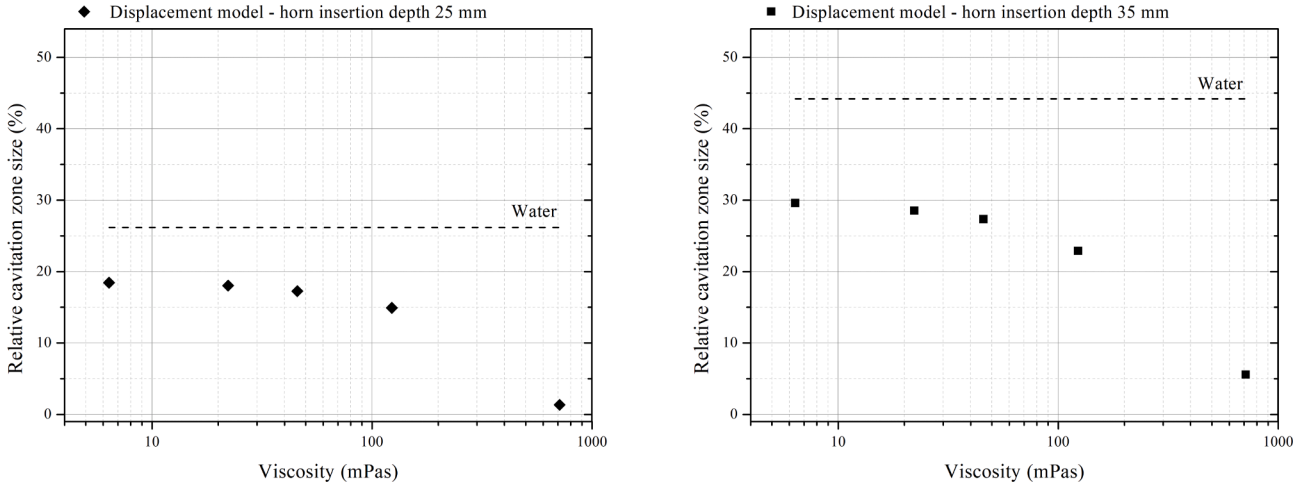

Fig. 11. Total cavitation zone size for increasing viscosity mixtures, liquid level of 60 mm, sonication power of 100% at horn insertion depth of 25 mm (left) and 35 mm (right). The intensity for water is plotted as reference in both figures.

The calorimetric power, following the electrical power, increases for viscosity up to ≈50 mPas but decreases for the highest viscosity samples, which is attributed to the poor heat diffusion associated with such viscous systems. The SCL results reveal that for the investigated system, two cavitational active zones exist. One is located directly at the tip of the horn and one along the body of the horn. Combination of the calorimetric and SCL results suggests that viscosity of approximately 50 mPas is a threshold viscosity region for the transition of cavitation activity, indicating alteration of the intensity of the bubbles oscillation and collapse. A strong jet is formed directly below the tip of the horn, and the velocity of the particles circulating in this region drops considerably when the medium changes from water to 123 mPas solution or when comparing only the PEG-water samples. Additionally, the motion of the particles becomes more laminar with increase in viscosity of the solutions. The version of the numerical simulation that accounts for both axial and radial horn movement is found to compare better to experimental results. This model is able to predict the cavitation zones location, is robust when the horn insertion depth is modified and is able to illustrate the impact of viscosity in the cavitation activity in the reactor.

The obtained results are a solid basis towards understanding the effects of ultrasound in high viscosity environments and form concrete recommendations for practical aspects when designing a sonication system for production of high viscosity products. The horn insertion depth for example, is proved to be a crucial parameter to be taken into consideration because above a specific insertion ratio (≈50-60% of the liquid height or wavelength in the chosen system) a second cavitationally active zone appears. It is therefore recommended to consider this increase in sonication area more carefully in high viscosity applications since this can be helpful during the first minutes of a polymerization by improving the dispersion of the reactants. The second active zone should be anticipated specially when scaling up strategies are developed. In addition, the PIV results indicated that for higher viscosities the US mixing intensity decreases, therefore either multiple horns should be used simultaneously –for example, for local reaction activation, or a combination of horns and impellers– for achieving global convective mixing in the vessel.

Some improvements that can be made in further investigations are foreseen. These include a more elaborate damping model, solid mechanics and acoustic streaming incorporation in the model and the validation against available experimental results. Further insights are also expected into the role of the radial horn displacement, both in the energy and pressure distribution in the reactor.

CRediT authorship contribution statement

Ariana Bampouli: Conceptualization, Methodology, Investigation, Data curation, Validation, Visualization, Writing – original draft, Writing – review & editing. **Quinten Goris:** Investigation, Data curation, Writing – original draft. **Jonas Van Olmen:** Investigation, Data curation, Writing – original draft. **Serkan Solmaz:** Investigation, Data curation, Writing – review & editing. **Mohammed Noorul Hussain:** Investigation, Data curation, Writing – review & editing. **Georgios D. Stefanidis:** Methodology, Writing – review & editing, Supervision, Funding acquisition. **Tom Van Gerven:** Conceptualization, Methodology, Project administration, Resources, Writing – review & editing, Supervision, Funding acquisition.

Declaration of Competing Interest

The authors declare that they have no known competing financial interests or personal relationships that could have appeared to influence the work reported in this paper.

Acknowledgments

Funding by the European Union's Horizon research and innovation programmes is gratefully acknowledged by Ariana Bampouli for the SIMPLIFY project (grant agreement No 820716) and Quinten Goris for the SIMPLI-DEMO project (grant agreement No 101058279). Jonas Van Olmen acknowledges support from the Research Foundation – Flanders (FWO), project G0D7421N and Mohammed Noorul Hussain for the VLAIO (Catalisti) in the MMICAS project HBC.2020.2627.

We would like to thank professor Wübbenhorst from the department of Physics and Astronomy of KU Leuven for providing access to the equipment for the speed of sound measurements and Dr. Helge Pfeiffer for the insightful discussions. In addition, the department of Soft Matter, Rheology and Technology of KU Leuven for providing access to the DSC equipment, the department of Chemistry of KU Leuven for providing access to the viscodensity meter and the tensiometer. We are also grateful to professor Simon Kuhn and Keiran Mc Carogher from the ProcESS engineering for Sustainable systems of KU Leuven for the help and the support during the PIV measurements. Finally, we would like to thank Weber Ultrasonics for the measurement of the horn axial displacement.

Appendix A. Supplementary data

Supplementary data to this article can be found online at https://doi.org/10.1016/j.ultsonch.2023.106444.

References

[1] V.S. Sutkar, P.R. Gogate, Design aspects of sonochemical reactors: Techniques for understanding cavitational activity distribution and effect of operating parameters, Chem. Eng. J. 155 (1–2) (2009) 26–36.
[2] S. Koda and K. Yasuda, Sonochemical Engineering Processes. Elsevier Inc., 2015.
[3] K.S. Suslick, G.J. Price, Applications of ultrasound to materials chemistry, Annu. Rev. Mater. Sci. 29 (1) (Aug. 1999) 295–326.
[4] G.J. Price, D.J. Norris, P.J. West, Polymerization of methyl methacrylate initiated by ultrasound, Macromolecules 25 (24) (Nov. 1992) 6447–6454.
[5] P. Kruus, T.J. Patraboy, Initiation of polymerization with ultrasound in methyl methacrylate, J. Phys. Chem. 89 (15) (Jul. 1985) 3379–3384.
[6] H. Nomura and S. Koda, What Is Sonochemistry? Elsevier Inc., 2015.
[7] J. Klíma, A. Frias-Ferrer, J. González-García, J. Ludvík, V. Sáez, J. Iniesta, Optimisation of 20 kHz sonoreactor geometry on the basis of numerical simulation of local ultrasonic intensity and qualitative comparison with experimental results, Ultrason. Sonochem. 14 (1) (2007) 19–28.
[8] S. Dähnke, F.J. Keil, Modeling of three-dimensional linear pressure fields in sonochemical reactors with homogeneous and inhomogeneous density distributions of cavitation bubbles, Ind. Eng. Chem. Res. 37 (3) (1998) 848–864.
[9] V.S. Sutkar, P.R. Gogate, L. Csoka, Theoretical prediction of cavitational activity distribution in sonochemical reactors, Chem. Eng. J. 158 (2) (2010) 290–295.
[10] R. Jamshidi, B. Pohl, U.A. Peuker, G. Brenner, Numerical investigation of sonochemical reactors considering the effect of inhomogeneous bubble clouds on ultrasonic wave propagation, Chem. Eng. J. 189–190 (2012) 364–375.
[11] I. Garcia-Vargas, L. Barthe, P. Tierce, O. Louisnard, Simulations of a full sonoreactor accounting for cavitation, Ultrason. Sonochem. 91 (October) (2022) 106226.
[12] Y.C. Wang, M.C. Yao, Realization of cavitation fields based on the acoustic resonance modes in an immersion-type sonochemical reactor, Ultrason. Sonochem. 20 (1) (2013) 565–570.
[13] T.J. Mason, J.P. Lorimer, Applied Sonochemistry: The Uses of Power Ultrasound in Chemistry and Processing, vol. 0, Wiley-VCH Verlag GmbH, 2002.
[14] B.J. Exsted, M.W. Urban, Grafting of silicon phthalocyanine dichloride onto poly (vinylidene fluoride) film surfaces by ultrasound, J. Inorg. Organomet. Polym. 3 (2) (1993) 105–127.
[15] S. Dähnke, K.M. Swamy, F.J. Keil, Modeling of three-dimensional pressure fields in sonochemical reactors with an inhomogeneous density distribution of cavitation bubbles. Comparison of theoretical and experimental results, Ultrason. Sonochem. 6 (1–2) (Mar. 1999) 31–41.
[16] L.V. Wijngaarden, One-dimensional flow of liquids containing small gas bubbles, Annu. Rev. Fluid Mech. 4 (1) (1972) 369–396.
[17] R.E. Caflisch, M.J. Miksis, G.C. Papanicolaou, L. Ting, Effective equations for wave propagation in bubbly liquids, J. Fluid Mech. 153 (1985) 259–273.
[18] O. Louisnard, A simple model of ultrasound propagation in a cavitating liquid. Part II: primary Bjerknes force and bubble structures, Ultrason. Sonochem. 19 (1) (2012) 56–65.
[19] K.W. Commander, A. Prosperetti, Linear pressure waves in bubbly liquids: comparison between theory and experiments, J. Acoust. Soc. Am. 85 (2) (1989) 732–746.
[20] Z. Wei, L.K. Weavers, Combining COMSOL modeling with acoustic pressure maps to design sono-reactors, Ultrason. Sonochem. 31 (2016) 490–498.
[21] O. Louisnard, I. Garcia-Vargas, Simulation of sonoreators accounting for dissipated power, First Edit. Elsevier Ltd. (2022).
[22] D. Rossi, R. Jamshidi, N. Saffari, S. Kuhn, A. Gavriilidis, L. Mazzei, Continuous-flow sonocrystallization in droplet-based microfluidics, Cryst. Growth Des. 15 (11) (2015) 5519–5529.
[23] C. Delacour, D.S. Stephens, C. Lutz, R. Mettin, S. Kuhn, Design and characterization of a scaled-up ultrasonic flow reactor, Org. Process Res. Dev. 24 (10) (2020) 2085–2093.
[24] O. Assia, D. Hakim, Propagation of Ultrasonic Waves in Viscous Fluids, IntechOpen, London, United Kingdom, 2010.
[25] S.L. Garrett Understanding Acoustics: An Experimentalist's View of Sound and Vibration Graduate Texts in Physics 2nd ed. 2020 Springer Cham.
[26] J.D.N. Cheeke, Fundamentals and applications of ultrasonic waves, CRC Press, Boca Raton, 2002.
[27] S. Dähnke, K.M. Swamy, F.J. Keil, A comparative study on the modeling of sound pressure field distributions in a sonoreactor with experimental investigation, Ultrason. Sonochem. 6 (4) (1999) 221–226.
[28] J. Jordens, A. Honings, J. Degrève, L. Braeken, T. Van Gerven, Investigation of design parameters in ultrasound reactors with confined channels, Ultrason. Sonochem. 20 (6) (2013) 1345–1352.
[29] V. Salinas, Y. Vargas, O. Louisnard, L. Gaete, Influence of the liquid viscosity on the formation of bubble structures in a 20 kHz field, Ultrason. Sonochem. 22 (2015) 227–234.
[30] H. Pfeiffer, G. Klose, K. Heremans, C. Glorieux, Thermotropic phase behaviour of the pseudobinary mixtures of DPPC/C 12E5 and DMPC/C12E5 determined by differential scanning calorimetry and ultrasonic velocimetry, Chem. Phys. Lipids 139 (1) (2006) 54–67.
[31] E. Hanke, U. Schulz, U. Kaatze, Molecular interactions in poly(ethylene glycol)-water mixtures at various temperatures: Density and isentropic compressibility study, ChemPhysChem 8 (4) (2007) 553–560.
[32] J. Lubbers, R. Graaff, A simple and accurate formula for the sound velocity in water, Ultrasound Med. Biol. 24 (7) (1998) 1065–1068.
[33] A.J. Sojahrood, H. Haghi, R. Karshafian, M.C. Kolios, Classification of the major nonlinear regimes of oscillations, oscillation properties, and mechanisms of wave energy dissipation in the nonlinear oscillations of coated and uncoated bubbles, Phys. Fluids 33 (1) (2021) pp.
[34] S.W. Dähnke, F.J. Keil, Modeling of linear pressure fields in sonochemical reactors considering an inhomogeneous density distribution of cavitation bubbles, Chem. Eng. Sci. 54 (13–14) (1999) 2865–2872.
[35] F.J. Trujillo, A strict formulation of a nonlinear Helmholtz equation for the propagation of sound in bubbly liquids. Part I: theory and validation at low acoustic pressure amplitudes, Ultrason. Sonochem. 47 (September) (2017, 2018,) 75–98.
[36] J.K. Chu, T.J. Tiong, S. Chong, U.A. Asli, Investigation on different time-harmonic models using FEM for the prediction of acoustic pressure fields in a pilot-scale sonoreactor, Chem. Eng. Sci. 247 (2021), 116912.
[37] COMSOL, "Acoustics Module User's Guide." [Online]. Available: https://doc.comsol.com/5.4/doc/com.comsol.help.aco/AcousticsModuleUsersGuide.pdf.
[38] G. Dukhin, in: "Fundamentals of acoustics in liquids.", in *Ultrasound for Characterizing Colloids*, Elsevier, 2002, pp. 75–99.
[39] G.S.B. Lebon, I. Tzanakis, K. Pericleous, D. Eskin, P.S. Grant, Ultrasonic liquid metal processing: The essential role of cavitation bubbles in controlling acoustic streaming, Ultrason. Sonochem. 55 (September) (2018, 2019,) 243–255.
[40] V. Sáez, A. Frías-Ferrer, J. Iniesta, J. González-García, A. Aldaz, E. Riera, Chacterization of a 20 kHz sonoreactor. Part I: analysis of mechanical effects by classical and numerical methods, Ultrason. Sonochem. 12 (1-2) (2005) 59–65.

[41] N.J. Watson, Ultrasound tomography, Elsevier Ltd, 2015.
[42] Hielscher Ultrasonics, "Application of Power Ultrasound using Ultrasonic Horns." [Online]. Available: https://www.hielscher.com/application-of-power-ultrasound-using-ultrasonic-horns.htm. [Accessed: 07-Dec-2022].
[43] Y. Son, Y. No, J. Kim, Geometric and operational optimization of 20-kHz probe-type sonoreactor for enhancing sonochemical activity, Ultrason. Sonochem. vol. 65, no. January (2020), 105065.
[44] K. Fattahi, E. Robert, D.C. Boffito, Numerical and experimental investigation of the cavitation field in horn-type sonochemical reactors, Chem. Eng. Process. - Process Intensif. vol. 182, no. June (2022), 109186.
[45] S. Hilgenfeldt, M.P. Brenner, S. Grossmann, D. Lohse, Analysis of Rayleigh-Plesset dynamics for sonoluminescing bubbles, J. Fluid Mech. 365 (1917) (1998) 171–204.
[46] O. Louisnard, A viable method to predict acoustic streaming in presence of cavitation, Ultrason. Sonochem. 35 (2017) 518–524.
[47] Y. Fang, T. Yamamoto, S. Komarov, Cavitation and acoustic streaming generated by different sonotrode tips, Ultrason. Sonochem. 48 (May) (2018) 79–87.
[48] S. Lesnik, A. Aghelmaleki, R. Mettin, G. Brenner, Modeling acoustic cavitation with inhomogeneous polydisperse bubble population on a large scale, Ultrason. Sonochem. vol. 89, no. May (2022), 106060.
[49] T. Yamamoto, K. Kubo, S.V. Komarov, Characterization of acoustic streaming in water and aluminum melt during ultrasonic irradiation, Ultrason. Sonochem. 71 (June 2020) (2021) 105381.
[50] I. Tzanakis, G.S.B. Lebon, D.G. Eskin, K.A. Pericleous, Characterizing the cavitation development and acoustic spectrum in various liquids, Ultrason. Sonochem. 34 (2017) 651–662.
[51] T. Nowak, C. Cairós, E. Batyrshin, R. Mettin, Acoustic streaming and bubble translation at a cavitating ultrasonic horn, AIP Conf. Proc. 1685 (2015).
[52] A. Mandroyan, M.L. Doche, J.Y. Hihn, R. Viennet, Y. Bailly, L. Simonin, Modification of the ultrasound induced activity by the presence of an electrode in a sono-reactor working at two low frequencies (20 and 40 kHz). Part II: mapping flow velocities by particle image velocimetry (PIV), Ultrason. Sonochem. 16 (1) (2009) 97–104.
[53] M. N. Shneider and M. Pekker, "Surface tension of small bubbles and droplets and the cavitation threshold," Jan. 2019.
[54] F.R. Young, Sonoluminescence from glycerine-water mixtures, Nature 206 (4985) (1965) 706.
[55] K. Yasui, A. Towata, T. Tuziuti, T. Kozuka, K. Kato, Effect of static pressure on acoustic energy radiated by cavitation bubbles in viscous liquids under ultrasound, J. Acoust. Soc. Am. 130 (5) (2011) 3233–3242.
[56] M. Ashokkumar, The characterization of acoustic cavitation bubbles - an overview, Ultrason. Sonochem. 18 (4) (2011) 864–872.